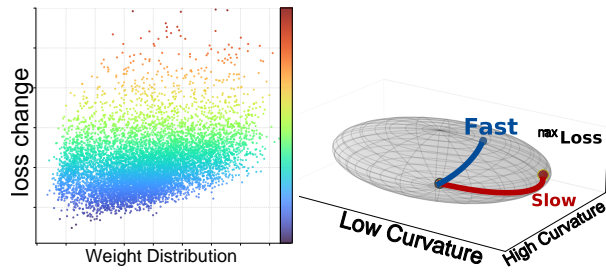


HeRo-Q: A General Framework for Stable Low Bit Quantization via Hessian Conditioning

Jinhao Zhang¹ Yunquan Zhang² Zicheng Yan³ Boyang Zhang^{4,5} Jun Sun⁶ Daning Cheng²

Abstract

Post-Training Quantization (PTQ), a mainstream model compression technique, often leads to the paradoxical “low-error, high-loss” phenomenon because it focuses solely on minimizing quantization error. The root cause lies in the Hessian matrix of the LLM loss landscape: a few high-curvature directions are extremely sensitive to perturbations. To address this, we propose the Hessian Robust Quantization (HeRo-Q) algorithm, which applies a lightweight, learnable rotation-compression matrix to the weight space prior to quantization. This joint framework reshapes the loss landscape by reducing the largest Hessian eigenvalue and reducing its max eigenvalue, thereby significantly enhancing robustness to quantization noise. HeRo-Q requires no architectural modifications, incurs negligible computational overhead, and integrates seamlessly into existing PTQ pipelines. Experiments on Llama and Qwen models show that HeRo-Q consistently outperforms state-of-the-art methods—including GPTQ, AWQ, and SpinQuant—not only achieving superior performance under standard W4A8 settings, but also excelling in the highly challenging W3A16 ultra-low-bit regime, where it boosts GSM8K accuracy on Llama-3-8B to 70.15% and effectively avoids the logical collapse commonly seen in aggressive quantization.



(a) low-error, high-loss for some weight parameters (b) local geometry of the loss landscape

Figure 1. a: Certain parameters suffer severe performance degradation even under small quantization noise because their noise components project significantly onto the high-curvature (short-axis) directions. Noise amplitude is fixed across all trials in the figure. b: The local geometry of the loss landscape around a converged point can be approximated by a hyper-ellipsoid: its short axis corresponds to the direction of the largest Hessian eigenvalue (high curvature). In contrast, its long axis aligns with the smallest eigenvalue (low curvature). A small perturbation along the short axis causes a dramatic increase in loss, whereas a perturbation of the same magnitude along the long axis has a negligible effect.

1. Introduction

Post-Training Quantization (PTQ) is a key technology nowadays. Current mainstream PTQ methods primarily aim to minimize quantization error. They typically employ symmetric or asymmetric linear mapping schemes, use a calibration dataset to estimate dynamic ranges, and select optimal quantization parameters by minimizing statistical discrepancies between pre-quantized and post-quantized weights or activations.

Although these strategies work well for traditional models

¹Beijing University of Posts and Telecommunications, Beijing, China ²Institute of Computing Technology, Chinese Academy of Sciences, Beijing, China ³University of Science and Technology of China, Hefei, China ⁴Peng Cheng Laboratory, Shenzhen, China ⁵University of Chinese Academy of Sciences, Beijing, China ⁶Zhejiang University, Hangzhou, China. Correspondence to: Firstname1 Lastname1 <firstname.lastname@xxx.edu>.

like those in computer vision, they often encounter a “low-error, high-loss” paradox when applied to modern LLMs: even with extremely low overall quantization error, downstream task performance can still degrade substantially, as shown in Figure 1a. This suggests the existence of highly sensitive parameters that, despite contributing little to overall noise, exert a disproportionately large impact on model behavior.

The root cause of this degradation lies in the geometric structure of the LLM loss landscape—particularly the ill-conditioned nature of its Hessian matrix. Specifically, the Hessian spectrum of LLMs is highly non-uniform: a few directions exhibit very large eigenvalues (i.e., high curvature), while most directions have near-zero eigenvalues (i.e., flat regions). This strong anisotropy makes the model exquisitely sensitive to tiny perturbations along high-curvature directions. Since quantization noise is injected uniformly across all dimensions, even minimal total noise can cause significant performance collapse if it has any non-zero component along these sensitive directions, as shown in Figure 1b.

Therefore, the key to enhancing the stability of model quantization lies in reducing the large eigenvalues of the Hessian matrix through low-cost transformations.

In this paper, we propose the Hessian Robust Quantization (HeRo-Q) algorithm, a novel quantization framework. Instead of directly minimizing quantization error, HeRo-Q reconstructs the weight space via a synergistic joint transformation strategy. Specifically, the diagonal smoothing component actively compresses the Hessian’s spectral radius to tame the outlier curvature, while the learnable orthogonal rotation redistributes quantization noise across dimensions to minimize its alignment with high-sensitivity directions. By decoupling these geometric roles, HeRo-Q effectively lowers the model’s worst-case sensitivity to quantization perturbations. Importantly, HeRo-Q requires no changes to model architecture or activation functions—it introduces only a lightweight, learnable linear transformation on weights, making it fully compatible with existing PTQ pipelines for fast and effective quantization, shown in Figure 2.

Our contributions are as follows: (1) We establish a theoretical connection between quantization robustness and Hessian spectral properties from the perspective of loss landscape geometry, and propose the HeRo-Q algorithm accordingly; (2) HeRo-Q applies only a single learnable matrix multiplication before quantization, incurring negligible extra computational cost; (3) In experiments, HeRo-Q consistently outperforms state-of-the-art PTQ methods (e.g., GPTQ, AWQ, SpinQuant) on both Llama and Qwen model families. It achieves superior language modeling and reasoning accuracy under different quantization configurations with low inference cost.

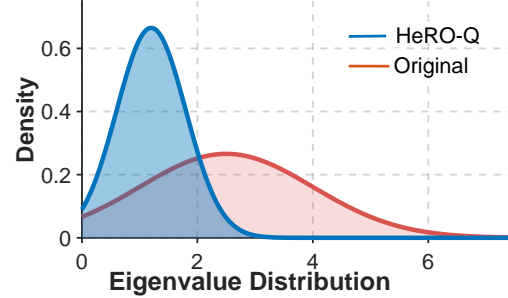


Figure 2. HeRo-Q stabilizes quantization by reshaping the Hessian spectrum. Through a lightweight linear transformation, HeRo-Q attenuates large eigenvalues—particularly outliers far from the bulk of the spectrum—and caps the maximum eigenvalue, thereby reducing the loss landscape’s sensitivity to quantization noise and enabling robust, efficient low-bit inference.

2. Related Work

Contemporary quantization strategies diverge sharply in how they allocate numerical precision across neural networks. On one end of the spectrum lie uniform-bitwidth approaches, which—despite their simplicity—impose a single precision level globally (see, e.g., (Zhang et al., 2024a; Zhang et al.; 2024b; 2025a;b; 2026)). While easy to implement, they often sacrifice performance for consistency. In response, mixed-precision schemes emerged, dynamically tailoring bit-widths per layer to strike a nuanced compromise between computational thrift and predictive fidelity.

Search-driven quantization frames bit-width assignment as a combinatorial optimization problem, with methods like AutoQ (Lou et al., 2019), HAQ (Wang et al., 2019), and mixed-precision schemes (Wu et al., 2018) iteratively exploring precision configurations guided by accuracy or loss to find Pareto-optimal solutions—yet their exhaustive search is computationally prohibitive for large models. Sensitivity-aware quantization offers a more efficient alternative by compressing layers according to their error tolerance: robust layers use low precision, while sensitive ones retain higher bit-widths. Layer sensitivity is estimated via metrics such as KL divergence (Cai et al., 2020; Xu et al., 2024), Hessian-based curvature (Dong et al., 2020; Yao et al., 2021), Gauss–Newton approximations (Chen et al., 2021), or custom scores (Tang et al., 2022), all aiming to minimize total network sensitivity under a fixed compression budget.

Beneath these algorithmic innovations lies a bedrock of foundational techniques that reshape post-training quantization. AdaRound (Nagel et al., 2020) rethinks rounding as a learnable reconstruction task; GPTQ (Frantar et al., 2022) and AWQ (Lin et al., 2024) demonstrate that preserving salient weights or activating outlier-aware scaling can rescue ultra-low-bit performance; SmoothQuant (Xiao

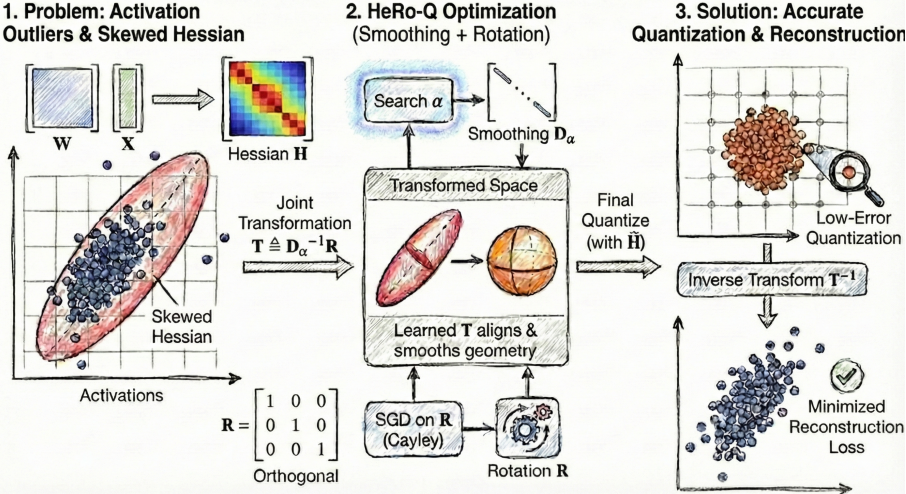


Figure 3. Robust Quantization via Hessian Transformation: HeRo-Q first analyzes the Hessian structure and identifies a severe Hessian geometric skewness—certain directions exhibit extremely high curvature (corresponding to large eigenvalues) and are highly sensitive to quantization noise. To address this, HeRo-Q searches over smoothing parameters α to construct a diagonal scaling matrix \mathbf{D}_α , and learns an orthogonal rotation matrix \mathbf{R} via the Cayley transform. Together, they form a linear transformation $\mathbf{T} = \mathbf{D}_\alpha^{-1}\mathbf{R}$ that maps the original weight space into a geometrically more balanced transformed space. Robust quantization is then performed in this transformed space, and the quantized weights in the original space are recovered through the inverse transformation.

et al., 2023) tames activation outliers through input-aware rescaling. The latest wave pushes further: QuIP (Chee et al., 2023) injects incoherence to stabilize extreme quantization; OmniQuant (Shao et al., 2024) makes clipping thresholds trainable; and SpinQuant (Liu et al., 2025) preprocesses weights with optimized rotation matrices to suppress outliers before quantization even begins—turning geometry into a weapon against information loss.

3. Methodology

3.1. Notation

In this section, we list all notations in our paper, including the Appendix.

- \mathbf{H} : Original Hessian Matrix.
- $\tilde{\mathbf{H}}$: Transformed Hessian Matrix.
- λ_{\max} : The magnitude of the spectral radius.
- α : Smoothing Hyperparameter ($\alpha \in [0, 1]$).
- $\Delta\mathcal{L}$: Loss degradation caused by quantization.
- \mathbf{w} : Pre-trained full-precision weights, $\mathbf{w} \in \mathbb{R}^d$.
- $\hat{\mathbf{w}}$: Quantized weights.
- $\boldsymbol{\delta}$: The quantization perturbation vector.
- $\mathcal{B}(\alpha)$: The spectral error bound governed by α .
- \mathbf{R} : An orthogonal rotation matrix ($\mathbf{R}^\top \mathbf{R} = \mathbf{I}$).

- \mathbf{D}_α : The diagonal smoothing matrix associated with parameter α .

3.2. Motivation

We establish the relationship among the spectrum of the Hessian matrix, the noise introduced by quantization, and the resulting change in the loss function through the following Theorem 3.1. The proof is shown in Appendix A.4.

Since the pre-trained model resides in a local minimum, the Hessian is positive semi-definite, ensuring $\lambda_{\max} > 0$. We introduce the smoothing coefficient α to control the intensity of diagonal smoothing. It acts as a tuning knob, balancing the trade-off between ‘compressing the Hessian spectral radius’ and ‘reducing clipping errors’.

Theorem 3.1 (Spectral Surrogate Bound). *By introducing a smoothing hyperparameter α (defined in Eq. 4) to regulate the Hessian spectral distribution, the loss variation induced by quantization admits the following quadratic surrogate upper bound:*

$$\Delta\mathcal{L}_{\text{quad}} \leq \frac{1}{2}\lambda_{\max}(\mathbf{H})\|\boldsymbol{\delta}\|_2^2 \leq \frac{1}{2}\|\boldsymbol{\delta}\|_2^2 \cdot \mathcal{B}(\alpha). \quad (1)$$

Here, $\mathcal{B}(\alpha)$ denotes a spectral surrogate metric defined on the transformed Hessian $\tilde{\mathbf{H}}$:

$$\mathcal{B}(\alpha) \triangleq \max_k \left(|H_{kk}|^{1-\alpha} + \sum_{j \neq k} |\hat{H}_{kj}| \right). \quad (2)$$

This bound characterizes how partial spectral smoothing reshapes the effective curvature of the quadratic approxi-

mation, providing a theoretical explanation for the reduced sensitivity to perturbations observed in practice.

In Large Language Models such as Llama-3 3B, the Hessian matrix exhibits an extremely pathological ‘long-tail’ distribution, resulting in a substantial magnitude of the spectral radius λ_{\max} . According to Theorem 3.1, the upper bound of the quantization error is jointly determined by the quantization noise $\|\delta\|$ and the spectral bound term $\mathcal{B}(\alpha)$. Given the excessive magnitude of the spectral radius λ_{\max} in LLMs, it effectively supersedes the quantization noise $\|\delta\|$ as the dominant factor governing the quantization error.

However, existing quantization strategies often overlook this geometric property—in the presence of a massive spectral radius λ_{\max} , the contribution of merely reducing the noise norm towards error suppression is negligible.

3.3. HeRo-Q Algorithm

To address the numerical instability induced by excessively large eigenvalues of the Hessian, we propose the Hessian Robust Quantization algorithm, shown in Algorithm 1, a novel post-training quantization framework that actively reshapes the loss landscape prior to quantization. The work pattern of HeRo-Q is shown in Figure 3. The core idea is to precondition the Hessian geometry via an optimal linear transformation, thereby suppressing its spectral radius and stabilizing quantization.

In our algorithm, let the transformed equivalent Hessian be $\tilde{\mathbf{H}} \triangleq \mathbf{T}^\top \mathbf{H} \mathbf{T}$. Guided by Theorem 3.1, which bounds the quantization-induced loss perturbation by a function $\mathcal{B}(\alpha)$ dependent on the Hessian spectrum, we design \mathbf{T} to minimize this bound. To this end, we decompose spectral compression into two synergistic operations: *diagonal smoothing* to tame outlier curvature, and *orthogonal rotation* to redistribute energy across dimensions. Specifically, we define:

$$\mathbf{T} \triangleq \mathbf{D}_\alpha^{-1} \mathbf{R}, \quad (3)$$

where $\mathbf{R} \in \mathbb{R}^{d \times d}$ is an orthogonal rotation matrix ($\mathbf{R}^\top \mathbf{R} = \mathbf{I}$), and \mathbf{D}_α is a diagonal smoothing matrix constructed from the absolute values of the Hessian diagonal:

$$\mathbf{D}_\alpha = \text{diag} \left(|H_{11}|^{\alpha/2}, |H_{22}|^{\alpha/2}, \dots, |H_{dd}|^{\alpha/2} \right), \quad (4)$$

with $\alpha \in [0, 1]$ acting as a tunable hyperparameter that controls the aggressiveness of outlier suppression—effectively serving as a *spectral equalizer*.

The theoretical justification for this design is provided by the following result:

Theorem 3.2 (Strict Reduction of Spectral Error Bound). *Under the long-tail Hessian assumption (i.e., there exists k such that $|H_{kk}| \gg 1$),*

$$\exists \alpha^* \in (0, 1) \text{ s.t. } \mathcal{B}(\alpha^*) < \mathcal{B}(0). \quad (5)$$

This result implies that Hessian spectral reduction strictly tightens the theoretical upper bound of the spectral error compared to the unsmoothed baseline ($\alpha = 0$). This strictly improved bound serves as the theoretical motivation for the robustness observed in our method.

This theorem confirms that attenuating dominant diagonal entries via smoothing strictly reduces the spectral error bound. Building on this geometric insight, HeRo-Q implements a practical algorithm that searches for the optimal α^* to minimize this bound, while simultaneously learning an orthogonal rotation \mathbf{R}^* to align the quantization noise. Key hyperparameters are shown in the Appendix A.2.

HeRo-Q operates in three phases: First, it computes the diagonal of the Hessian matrix of input activations using calibration data to capture the sensitivity of each channel to the loss function. Second, for each candidate smoothing exponent α in a predefined search grid \mathcal{A} , it constructs a diagonal smoothing matrix $\mathbf{D}_\alpha = \text{diag}(|\mathbf{h}|^{\alpha/2})$ and combines it with a learnable orthogonal rotation matrix \mathbf{R} to form a joint transformation $\mathbf{T}(\mathbf{R}) = \mathbf{D}_\alpha^{-1} \mathbf{R}$. The rotation matrix is parameterized via the Cayley transform to preserve orthogonality and is optimized through gradient descent to minimize the Frobenius norm reconstruction error $\|\mathbf{XW} - \mathbf{XW}_{\text{sim}}\|_F^2$ between the original and quantized-simulated outputs. Finally, the algorithm selects the optimal pair (α^*, \mathbf{R}^*) that yields the lowest reconstruction error, applies the corresponding optimal transform $\mathbf{T}^* = \mathbf{D}_{\alpha^*}^{-1} \mathbf{R}^*$, and performs standard quantization to obtain high-fidelity quantized weights $\hat{\mathbf{W}}$. The standard quantization methods can be any quantization method, including GPTQ, RTN and so on.

3.4. Inference Efficiency

HeRo-Q employs a hybrid inference strategy that synergistically combines offline parameter fusion with optimized online computational kernels.

First, for the vast majority of linear layers in the model, we achieve strict zero computational overhead. We absorb the inverse of the smoothing matrix \mathbf{D}_α^{-1} directly into Normalization layers (LayerNorm or RMSNorm). This eliminates the need for any additional multiplication operators. For the dense rotation matrix \mathbf{R} learned via SGD, we fuse it offline into the adjacent weights ($\mathbf{W}_{\text{prev}} \leftarrow \mathbf{W}_{\text{prev}} \mathbf{R}$ and $\mathbf{W}_{\text{curr}} \leftarrow \mathbf{R}^\top \mathbf{W}_{\text{curr}}$), keeping the computational graph architecture unchanged.

Second, for components where weight fusion is inapplicable, such as KV Cache quantization or specific online activation processing, we follow the approach of SpinQuant (Liu et al., 2025) by adopting online Hadamard rotation. In this scenario, we utilize the Fast Walsh-Hadamard Transform (FWHT) kernel for efficient computation during infer-

Algorithm 1 HeRo-Q: Hessian Robust Quantization

```

1: Input: Pre-trained weights  $\mathbf{W}$ , Calibration inputs  $\mathbf{X}$ , Search
   grid  $\mathcal{A}$ , Bits  $b$ .
2: Output: Quantized weights  $\hat{\mathbf{W}}$ , Transform params  $\mathbf{D}_{\alpha^*}, \mathbf{R}^*$ .
3: for each Linear Layer do
4:   // Phase 1: Statistics Extraction
5:   Compute Hessian diag  $\mathbf{h} = \text{diag}(\mathbf{X}^\top \mathbf{X})$ .
6:   Init  $\mathcal{L}^* \leftarrow \infty, \alpha^* \leftarrow 0, \mathbf{R}^* \leftarrow \mathbf{I}$ .
7:   // Phase 2: Joint Optimization (Smoothing & Rotation)
8:   for  $\alpha \in \mathcal{A}$  do
9:     Construct smoothing matrix:  $\mathbf{D}_\alpha = \text{diag}(|\mathbf{h}|^{\alpha/2})$ .
10:    if layer is Online then
11:       $\mathbf{R} \leftarrow \mathbf{H}_{\text{Walsh}}$  {Use Fixed Hadamard for speed}
12:    else
13:      Init  $\mathbf{S}$ . for  $t = 1 \dots T_{\text{steps}}$  do {Learn  $\mathbf{R}$  via Cayley
        SGD}
14:         $\mathbf{R} \leftarrow (\mathbf{I} - \mathbf{S})(\mathbf{I} + \mathbf{S})^{-1}; \quad \mathbf{T} \leftarrow \mathbf{D}_\alpha^{-1} \mathbf{R}$ 
15:        Update  $\mathbf{S}$  to minimize  $\|\mathbf{XW} - \mathbf{X}(\mathbf{T} \cdot \text{Quant}(\mathbf{T}^{-1} \mathbf{W}))\|_F^2$ .
16:      end for
17:    end if
18:    // Quantize & Evaluate
19:     $\mathbf{T} \leftarrow \mathbf{D}_\alpha^{-1} \mathbf{R}; \quad \tilde{\mathbf{H}} = \mathbf{T}^\top \mathbf{H} \mathbf{T}$ .
20:     $\tilde{\mathbf{W}}_q \leftarrow \text{Quantization method}(\mathbf{T}^{-1} \mathbf{W}, \tilde{\mathbf{H}})$ .
21:     $\hat{\mathbf{W}}_{\text{rec}} \leftarrow \mathbf{T} \cdot \tilde{\mathbf{W}}_q$ .
22:    Compute MSE  $\mathcal{L} = \|\mathbf{XW} - \mathbf{X}\hat{\mathbf{W}}_{\text{rec}}\|_F^2$ .
23:    if  $\mathcal{L} < \mathcal{L}^*$  then
24:       $\mathcal{L}^* \leftarrow \mathcal{L}; \quad \alpha^* \leftarrow \alpha; \quad \mathbf{R}^* \leftarrow \mathbf{R}$ .
25:    end if
26:  end for
27:  // Phase 3: Final Quantization
28:  Apply optimal transform  $\mathbf{T}^* = \mathbf{D}_{\alpha^*}^{-1} \mathbf{R}^*$ .
29:  Return quantized weights  $\hat{\mathbf{W}}$  and parameters  $\mathbf{D}_{\alpha^*}, \mathbf{R}^*$ .
30: end for

```

ence. For a detailed time complexity analysis, please refer to Appendix A.7.

4. Experiments

In this section, we comprehensively validate the effectiveness and computational performance of the HeRo-Q algorithm through three experiments. First, in the downstream task evaluation, we assess model performance under various quantization configurations, including W4A4, W4A8, W4A16 and W3A16. Second, in the spectral analysis experiment, we demonstrate that HeRo-Q successfully realizes our key insight—effectively reducing the spectral radius of the Hessian matrix. Finally, in the computational performance evaluation, we show that models quantized with HeRo-Q achieve significantly higher inference throughput. Our code is shown in the Appendix A.1.

4.1. Experiments configuration

4.1.1. MODEL

We evaluate the proposed method on two representative model series: Llama-3-8B, Llama-3.2-1B, Llama-3.2-3B, Qwen2.5-3B, and Qwen2.5-7B.

4.1.2. DATASET

The language modeling tasks include C4 and WikiText2(wiki2), while the downstream tasks cover mathematical reasoning (GSM8K), commonsense reasoning (HellaSwag), and multi-task understanding (MMLU).

4.1.3. BENCHMARK

We benchmark our approach against SOTA methods, including GPTQ, AWQ, SmoothQuant, SpinQuant and Omni-Quant.

4.1.4. ALGORITHM PARAMETERS

In this experiment, all benchmark algorithms are configured with their default parameters as provided in their official implementations, while HeRo-Q selects the optimal smoothing hyperparameter α independently for each layer. We use GPTQ as standard quantization method in HeRo-Q in our experiments.

4.1.5. EVALUATION SETUP

For language modeling capabilities, we report the Perplexity (PPL) with a sequence length of 2048. To ensure a rigorous evaluation, the calibration dataset used for quantization is strictly separated from the evaluation dataset to prevent any data leakage. Furthermore, we assess downstream task performance following widely accepted evaluation protocols: MMLU (5-shot), GSM8K (8-shot), and HellaSwag (10-shot).

4.2. Downstream Task Evaluation

4.2.1. EVALUATION ON W4A8

Table 1 summarizes the comparative results under the standard W4A8 (4-bit weight, 8-bit activation) setting. HeRo-Q achieves consistent SOTA results across all tested models and metrics, fully validating the effectiveness of our method.

On Llama-3-8B, HeRo-Q reduces the WikiText-2 perplexity (PPL) to 6.96, significantly outperforming SpinQuant (7.48) and GPTQ (8.81), and extremely closely approaching the original FP16 precision (6.41). For the smaller Llama-3.2-1B model, our method also maintains the lowest PPL on the C4 dataset (22.84), superior to AWQ (23.97) and GPTQ (24.07).

Method	Llama-3-8B				Llama-3.2-1B				Llama-3.2-3B				Qwen2.5-3B				Qwen2.5-7B							
	C4↓	W2↓	GSM	HS	MMLU	C4↓	W2↓	GSM	HS	MMLU	C4↓	W2↓	GSM	HS	MMLU	C4↓	W2↓	GSM	HS	MMLU				
FP16	12.28	6.41	77.17	77.39	67.31	22.48	11.41	36.44	59.94	46.38	17.24	9.53	68.86	70.05	61.44	14.68	7.95	81.13	72.09	65.80				
AWQ	13.56	8.12	72.94	76.78	64.41	23.97	12.23	26.44	56.78	40.23	18.89	9.91	57.65	68.97	58.69	15.46	8.46	77.29	71.18	63.98				
GPTQ	14.12	8.81	71.89	76.91	60.54	24.07	12.18	24.24	57.04	40.58	18.99	9.82	55.75	68.35	57.16	15.65	8.87	76.44	70.74	63.25				
SmoothQuant	13.64	7.32	72.55	76.83	64.55	24.01	12.10	25.87	56.89	41.32	18.87	9.80	56.33	69.34	58.73	15.54	8.34	77.36	71.34	63.96				
SpinQuant	13.39	7.48	73.56	77.23	64.98	23.56	11.89	26.13	57.68	42.64	18.77	9.75	57.93	69.83	58.31	15.32	8.14	78.65	71.94	65.08				
HeRo-Q	12.94	6.96	75.26	77.28	66.31	22.84	11.67	31.43	57.98	43.77	17.87	9.73	61.81	69.97	59.87	14.98	8.01	79.68	72.01	65.49				
																				13.43	6.78	86.12	81.33	71.02

Table 1. Comprehensive performance comparison across Llama and Qwen series (W4A8). C4/W2 (Wiki2) are Perplexity (↓), others are Accuracy (↑).

Method	Llama-3-8B (W4A16)				Qwen-2.5-7B (W4A16)			
	W2↓	C4↓	MMLU	GSM	W2↓	C4↓	MMLU	GSM
FP16	6.41	12.28	67.31	77.17	6.66	13.26	71.48	87.96
GPTQ	6.65	12.55	65.80	74.20	6.95	13.85	69.80	85.20
AWQ	6.60	12.50	66.10	74.50	7.14	14.21	69.68	82.33
OmniQuant	6.48	12.35	66.80	75.80	6.75	13.40	70.90	86.80
SpinQuant	6.46	12.32	66.85	76.10	6.72	13.35	71.10	87.10
HeRo-Q	6.43	12.30	67.10	76.85	6.68	13.28	71.35	87.50

Table 2. W4A16 quantization performance

Method	Llama-3-8B (W3A16)				Llama-3.2-1B (W3A16)			
	W2↓	C4↓	MMLU	GSM	W2↓	C4↓	MMLU	GSM
FP16	6.41	12.28	67.31	77.17	11.41	22.48	46.38	36.44
GPTQ	20.13	28.94	25.12	26.30	41.30	65.80	14.20	5.10
AWQ	15.80	24.15	39.50	46.20	12.23	23.97	40.23	26.44
OmniQuant	9.45	15.80	59.80	63.50	17.50	32.10	36.50	21.40
SpinQuant	8.85	14.95	60.50	66.10	16.20	30.05	39.10	22.80
HeRo-Q	8.02	13.98	63.80	70.15	14.05	25.80	42.50	29.10

Table 3. W3A16 quantization performance

In downstream tasks, HeRo-Q demonstrates exceptional performance in tasks requiring rigorous logical reasoning and extensive knowledge.

Qwen2.5-7B: In the GSM8K mathematical reasoning benchmark, HeRo-Q achieves an accuracy of 86.12%, substantially leading SpinQuant (84.97%) and GPTQ (81.67%), effectively recovering the model’s complex reasoning capabilities. Meanwhile, in the MMLU task examining comprehensive knowledge, HeRo-Q also achieves a high score of 71.02%, nearly matching the FP16 baseline (71.48%).

Qwen2.5-3B: Even on the parameter-constrained 3B model, HeRo-Q remains robust. Its GSM8K accuracy reaches 79.68%, significantly outperforming GPTQ (76.44%) and SpinQuant (78.65%).

These results indicate that HeRo-Q can maintain language fluency and preserve the logical and cognitive capabilities of the model to a maximum across different architectures.

4.2.2. EVALUATION ON W4A16

Table 2 presents the detailed evaluation results under the W4A16 (4-bit weight, 16-bit activation) quantization configuration. In the W4A16 setting, HeRo-Q demonstrates remarkable performance recovery capabilities, achieving ‘near-lossless’ compression that is virtually indistinguishable from the FP16 original model.

For the Llama-3-8B model, our method achieves a PPL of 6.43 on WikiText-2, with a marginal gap of only 0.02 compared to the FP16 baseline (6.41). This high fidelity is simi-

larly reflected on the C4 dataset, where HeRo-Q achieves a PPL of 12.30, extremely close to the original value of 12.28, outperforming SpinQuant (12.32) and OmniQuant (12.35).

In downstream tasks, HeRo-Q demonstrates its protection of the model’s reasoning capabilities. On the Qwen-2.5-7B model, HeRo-Q achieves a score of 87.50% on the GSM8K mathematical reasoning task, preserving the reasoning ability of the original model (87.96%); on the MMLU comprehensive knowledge task, its score (71.35%) is also nearly identical to the FP16 performance (71.48%).

4.2.3. EVALUATION ON W3A16

To explore the performance boundaries of the algorithm in extreme compression scenarios, we conducted tests under the 3-bit weight (W3A16) setting (results are shown in Table 3). Under such conditions, traditional methods typically suffer from catastrophic performance degradation. For instance, on the Llama-3-8B model, the accuracy of GPTQ and AWQ on the GSM8K task plummets to 26.30% and 46.20%, respectively. This indicates that these methods fail to effectively preserve the model’s reasoning capabilities in such a sparsely quantized space, rendering the models practically unusable.

In contrast, our proposed HeRo-Q demonstrates robustness, maintaining a high accuracy of 70.15%. This result not only substantially surpasses traditional methods but also significantly outperforms the strongest current baselines, OmniQuant (63.50%) and SpinQuant (66.10%), achieving an absolute accuracy improvement of over 4%.

Regarding language modeling capabilities, HeRo-Q performs equally impressively. On Llama-3.2-1B, HeRo-Q reduces the Wiki2 perplexity (PPL) to 14.05, significantly superior to SpinQuant (16.20) and GPTQ (41.30).

4.2.4. EVALUATION ON W4A4

Method	Llama-3-8B (W4A4)		Llama-3.2-3B (W4A4)	
	Wiki2↓	C4↓	Wiki2↓	C4↓
FP16	6.41	12.28	9.53	17.24
AWQ	346	642.4	1000+	1000+
GPTQ	1000+	1000+	1000+	1000+
SmoothQuant	429	745	1000+	1000+
SpinQuant	12.14	17.46	15.31	25.41
HeRo-Q	10.29	14.84	13.18	20.14

Table 4. W4A4 quantization performance

Table 4 presents the performance comparison under the highly challenging W4A4 setting. As observed, the performance of most existing post-training quantization (PTQ) methods exhibits catastrophic collapse. The perplexity (PPL) of standard baselines such as AWQ, GPTQ, and SmoothQuant exceeds 1000. Although SpinQuant is able to retain certain linguistic capabilities, it still faces significant accuracy loss. In contrast, HeRo-Q consistently achieves the lowest perplexity across Llama-3-8B and Llama-3.2-3B models as well as Wiki2 and C4 datasets. Notably, in the Wiki2 test for Llama-3-8B, HeRo-Q achieved a perplexity of 10.29, significantly outperforming the runner-up method SpinQuant (12.14), effectively narrowing the gap with the original FP16 performance.

This robustness extends to the C4 dataset, where HeRo-Q reduces the PPL to 14.84, achieving a significant improvement of 2.62 over SpinQuant (17.46). Furthermore, on the Llama-3.2-3B model, which is more sensitive to quantization, HeRo-Q maintains a decisive advantage, outperforming SpinQuant by a margin of 5.27 on the C4 dataset (20.14 vs. 25.41). This fully demonstrates the consistent effectiveness of our method across different model scales.

4.3. Spectral Analysis Experiment

To verify the theoretical motivation behind HeRo-Q from an empirical perspective, we conducted a visual analysis of the Hessian eigenspectrum characteristics of the Llama-1B and Llama-3B models. Figure 4 and Figure 5 reveal how HeRo-Q eliminates the root cause of quantization error by reshaping the geometric structure.

Figure 4 displays the density distribution of the Hessian eigenspectrum. The distribution of the original model (red region) reveals the existence of a non-negligible portion of extreme eigenvalues in the LLM weight space, with magnitudes reaching up to $10^{7.6}$ (Llama-1B) and $10^{7.1}$ (Llama-3B). According to Theorem 3.1, these spectral outliers dominate the worst-case quantization error upper bound, making the model extremely sensitive to perturbations generated by low-bit quantization. The green distribution shows the effect of our method, HeRo-Q, after transformation. Our method not only shifts the distribution but also successfully compresses the spectral radius λ_{max} by approximately 3 to 4 orders of magnitude (e.g., reducing it from $10^{7.6}$ to $10^{4.0}$) by truncating the heavy tail. This drastic compression directly tightens the spectral error bound $\mathcal{B}(\alpha)$, effectively converting an ill-conditioned quantization problem into a well-conditioned one.

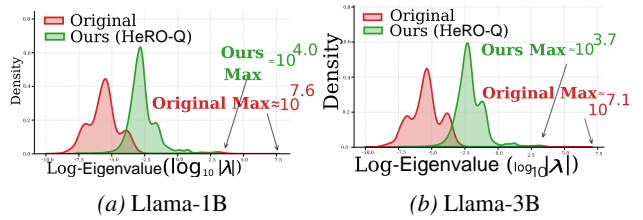


Figure 4. Global Hessian Eigenspectrum Transformation. Comparison of the log-magnitude density of Hessian eigenvalues before (Red) and after (Green) applying HeRo-Q on Llama-1B (a) and Llama-3B (b).

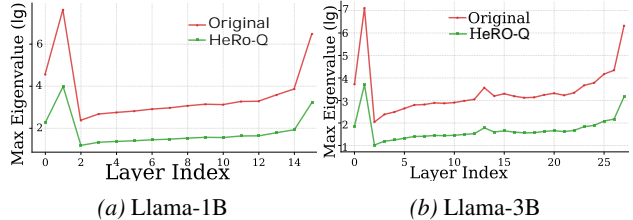


Figure 5. Layer-wise Spectral Radius (λ_{max}) Comparison. The original models (Red line) exhibit extreme volatility in spectral radius across layers, particularly in the embedding and output bottlenecks. HeRo-Q (Green line) acts as a spectral equalizer, consistently suppressing the peak curvature across all layers and reducing the variance of quantization difficulty.

Figure 5 provides a microscopic view of the distribution of λ_{max} on each network layer. The spectral characteristics of the original model (red line) exhibit severe volatility. Particularly in the initial embedding layers (indices 0-2) and the final output layers, there exist disproportionately high-curvature peaks. These layers constitute Bottlenecks: even if most layers in the network are well-quantized, these specific layers exponentially amplify the noise. This explains why traditional uniform quantization strategies often fail on specific layers. Our method, HeRo-Q (green line), acts as an efficient spectral equalizer. As shown in the figure, it consistently suppresses peaks across the entire network depth, significantly reducing the spectral radius. By reducing the inter-layer variance of λ_{max} , it guarantees the high performance of the model, enabling the model to avoid structural

collapse even under aggressive W3A16 quantization.

4.4. Computational Performance Evaluation

Method	Llama-1B	Llama-3B	Llama-8B
FP16	205.2Tokens/s	118.4Tokens/s	48.5Tokens/s
GPTQ	310.5Tokens/s	215.6Tokens/s	115.2Tokens/s
SpinQuant	302.8Tokens/s	209.5Tokens/s	112.8Tokens/s
HeRo-Q	303.1Tokens/s	210.0Tokens/s	113.1Tokens/s

Table 5. Real-world inference throughput on NVIDIA A800. Results are measured with W4A16 quantization.

The inference throughput results in Table 5 demonstrate the practical efficiency gains achieved by weight-only quantization under the W4A16 setting on an NVIDIA A800 GPU. All quantized methods—GPTQ, SpinQuant, and HeRo-Q—deliver substantial speedups over the FP16 baseline. Notably, HeRo-Q achieves throughput performance on par with or slightly better than SpinQuant (e.g., 113.1 vs. 112.8 Tokens/s on Llama-8B), while matching the high efficiency of GPTQ. This indicates that the spectral preconditioning introduced by HeRo-Q—despite its additional transformation overhead—does not compromise runtime performance. On the contrary, the negligible difference in speed relative to other SOTA methods suggests that the orthogonal rotation and diagonal smoothing operations are efficiently fused during deployment, enabling HeRo-Q to maintain competitive inference latency while offering improved accuracy.

4.5. Ablation Experiments

4.5.1. HYPERPARAMETER SENSITIVITY STUDY

α Strategy	Llama-3-8B		Qwen-2.5-7B	
	Wiki2 \downarrow	C4 \downarrow	Wiki2 \downarrow	C4 \downarrow
0.1	6.58	12.45	6.85	13.45
0.2	6.52	12.39	6.74	13.37
0.3	6.47	12.34	6.70	13.32
0.4	6.49	12.36	6.75	13.35
0.5	6.62	12.48	6.88	13.42
0.6	6.80	12.60	7.10	13.60
0.7	7.15	12.95	7.45	13.85
0.8	7.50	13.20	7.95	14.10
Layer-wise Opt. †	6.43	12.30	6.68	13.28

Table 6. We evaluate the perplexity (PPL) on Llama-3-8B and Qwen-2.5-7B under W4A16 quantization, confirming that $\alpha = 0.3$ provides the robust optimal balance between suppressing spectral outliers (left side) and minimizing distribution shift (right side).

To investigate the intrinsic mechanism of the smoothing factor α , we evaluated the PPL variations under different smoothing strengths $\alpha \in [0.1, 0.8]$, as detailed in Table

6. The numerical results reveal a distinct U-shaped trend, highlighting a competition between Hessian spectral radius compression and quantization clipping errors

In the lower α regime ($\alpha < 0.3$), the strength of the transformation matrix is insufficient to fully compress the maximum eigenvalue of the Hessian. This implies that those eigenvalues with large magnitudes remain unsuppressed. As predicted by Theorem 3.1, these unsuppressed eigenvalues magnify minute quantization errors into significant loss degradation.

Conversely, in the higher α regime, the PPL exhibits a gradually increasing trend. Although the Hessian spectral radius is forcefully suppressed, its inverse transformation leads to over-smoothing. This excessive smoothing causes the weight distribution to deviate from the optimal dynamic range of the linear quantization grid. Consequently, clipping errors rise sharply and supersede the Hessian spectral radius as the dominant factor affecting performance in this regime.

4.5.2. COMPONENT-WISE ANALYSIS

Method / Component	Configuration	Llama-3.2-1B (PPL)	Llama-3-8B (PPL)
FP16	Original	11.41	6.41
Baseline (GPTQ)	No	13.30	6.65
Smoothing Only	Only D_α	12.55	6.52
Rotation Only	Only R	12.11	6.49
HeRo-Q (Ours)	$D_\alpha + R$	11.94	6.43

Table 7. Ablation study of transformations on Llama models

We conducted a rigorous ablation study on Llama-3.2-1B and Llama-3-8B models (see Table 7) by imposing different mathematical constraints on the transformation matrix T to isolate variables.

Experimental results indicate that the untransformed Baseline (GPTQ) ($T = I$) exhibits a PPL as high as 13.30 on Llama-1B, confirming that the pathological nature of the original Hessian matrix and outliers hinder quantization performance. When we introduce the smoothing configuration (Smoothing-Only, $T \triangleq D_\alpha^{-1}$, forcing the constraint $R = I$), the Hessian-guided scaling reduces the PPL to 12.55, demonstrating that suppressing Hessian spectral outliers can reduce quantization error. However, this may induce distribution shifts, thereby limiting its performance upper bound. In comparison, the rotation configuration (Rotation-Only, $T \triangleq R$) demonstrates stronger gains than smoothing alone (PPL drops to 12.11). Yet, due to the lack of spectral radius compression, model performance remains severely affected. Finally, our proposed method HeRo-Q achieves the best performance across all metrics by removing all constraints and performing synergistic optimization ($T \triangleq D_\alpha^{-1}R$) (Llama-1B PPL of 11.94, Llama-8B PPL of 6.43).

5. Conclusion

This paper addresses the fundamental discrepancy in post-training quantization (PTQ) of large language models—wherein low quantization error frequently coincides with substantial degradation in task performance—by proposing HeRo-Q, a general and computationally efficient quantization framework. The core of HeRo-Q lies in a lightweight, learnable rotation-and-compression transformation applied before quantization, which actively reshapes the geometric structure of the weight space to reduce the spectral radius of the Hessian matrix of the loss landscape. Notably, HeRo-Q requires no architectural modifications, imposes negligible computational overhead, and integrates seamlessly into existing PTQ pipelines. Comprehensive empirical evaluations demonstrate that HeRo-Q consistently outperforms state-of-the-art quantization methods—including GPTQ, AWQ, and SpinQuant—across both standard (e.g., W4A8) and extremely aggressive (e.g., W3A16) low-bit quantization regimes.

6. Impact Statement

This work introduces HeRo-Q to enable high-fidelity, ultra-low-bit quantization for Large Language Models. By significantly reducing hardware barriers and energy consumption, our method promotes the democratization of AI, allowing powerful models to run on consumer-grade devices while supporting environmental sustainability. Furthermore, the improved quantization stability enhances the reliability of compressed models in practical applications. We do not foresee any specific ethical risks beyond those generally associated with large-scale model deployment.

References

Cai, Y., Yao, Z., Dong, Z., Gholami, A., Mahoney, M. W., and Keutzer, K. Zeroq: A novel zero shot quantization framework. In *Proceedings of the IEEE/CVF conference on computer vision and pattern recognition*, pp. 13169–13178, 2020.

Chee, J., Cai, Y., Kuleshov, V., and Sa, C. D. QuIP: 2-bit quantization of large language models with guarantees. In *Advances in Neural Information Processing Systems 36 (NeurIPS)*, 2023.

Chen, W., Wang, P., and Cheng, J. Towards mixed-precision quantization of neural networks via constrained optimization. In *Proceedings of the IEEE/CVF International Conference on Computer Vision*, pp. 5350–5359, 2021.

Dong, Z., Yao, Z., Arfeen, D., Gholami, A., Mahoney, M. W., and Keutzer, K. Hawq-v2: Hessian aware trace-weighted quantization of neural networks. *Advances in neural information processing systems*, 33:18518–18529, 2020.

Frantar, E., Ashkboos, S., Hoefer, T., and Alistarh, D. GPTQ: Accurate post-training quantization for generative pre-trained transformers. *arXiv preprint arXiv:2210.17323*, 2022.

Lin, J., Tang, J., Tang, H., Yang, S., Chen, W.-M., Wang, W.-C., Xiao, G., Dang, X., Gan, C., and Han, S. AWQ: Activation-aware weight quantization for on-device LLM compression and acceleration. In *Proceedings of the Seventh Annual Conference on Machine Learning and Systems (MLSys)*, 2024.

Liu, Z., Zhao, C., Fedorov, I., Soran, B., Choudhary, D., Krishnamoorthi, R., Chandra, V., Tian, Y., and Blankevoort, T. SpinQuant: LLM quantization with learned rotations. In *Proceedings of the Thirteenth International Conference on Learning Representations (ICLR)*, 2025.

Lou, Q., Guo, F., Liu, L., Kim, M., and Jiang, L. Autoq: Automated kernel-wise neural network quantization. *arXiv preprint arXiv:1902.05690*, 2019.

Nagel, M., Amjad, R. A., van Baalen, M., Louizos, C., and Blankevoort, T. Up or down? Adaptive rounding for post-training quantization. In *Proceedings of the 37th International Conference on Machine Learning (ICML)*, pp. 7197–7206, 2020.

Shao, W., Chen, M., Zhang, Z., Xu, P., Zhao, L., Li, Z., Zhang, K., Gao, P., Qiao, Y., and Luo, P. OmniQuant: Omnidirectionally calibrated quantization for large language models. In *Proceedings of the Twelfth International Conference on Learning Representations (ICLR)*, 2024.

Tang, C., Ouyang, K., Wang, Z., Zhu, Y., Ji, W., Wang, Y., and Zhu, W. Mixed-precision neural network quantization via learned layer-wise importance. In *European conference on computer vision*, pp. 259–275. Springer, 2022.

Wang, K., Liu, Z., Lin, Y., Lin, J., and Han, S. Haq: Hardware-aware automated quantization with mixed precision. In *Proceedings of the IEEE/CVF conference on computer vision and pattern recognition*, pp. 8612–8620, 2019.

Wu, B., Wang, Y., Zhang, P., Tian, Y., Vajda, P., and Keutzer, K. Mixed precision quantization of convnets via differentiable neural architecture search. *arXiv preprint arXiv:1812.00090*, 2018.

Xiao, G., Lin, J., Seznec, M., Wu, H., Demouth, J., and Han, S. SmoothQuant: Accurate and efficient post-training quantization for large language models. In *Proceedings of the 40th International Conference on Machine Learning (ICML)*, pp. 38087–38099, 2023.

Xu, K., Li, Z., Wang, S., and Zhang, X. Ptmq: Post-training multi-bit quantization of neural networks. In *Proceedings of the AAAI Conference on Artificial Intelligence*, volume 38, pp. 16193–16201, 2024.

Yao, Z., Dong, Z., Zheng, Z., Gholami, A., Yu, J., Tan, E., Wang, L., Huang, Q., Wang, Y., Mahoney, M., et al. Hawq-v3: Dyadic neural network quantization. In *International Conference on Machine Learning*, pp. 11875–11886. PMLR, 2021.

Zhang, B., Cheng, D., Zhang, Y., and Liu, F. Lod: Unlocking performance gains in compression via differential analysis.

Zhang, B., Cheng, D., Zhang, Y., and Liu, F. Fp= xint: A low-bit series expansion algorithm for post-training quantization. *arXiv preprint arXiv:2412.06865*, 2024a.

Zhang, B., Cheng, D., Zhang, Y., Liu, F., and Chen, W. Compression for better: A general and stable lossless compression framework. *arXiv preprint arXiv:2412.06868*, 2024b.

Zhang, B., Cheng, D., and Zhang, Y. Rethinking parameter sharing as graph coloring for structured compression. *arXiv preprint arXiv:2511.06786*, 2025a.

Zhang, J., Zhang, Y., Zhang, B., Liu, Z., and Cheng, D. Moqe: Improve quantization model performance via mixture of quantization experts. *arXiv preprint arXiv:2508.09204*, 2025b.

Zhang, J., Zhang, Y., Chen, D., JunSun, and Yan, Z. Calm: A cka-guided adaptive layer-wise modularization framework for llm quantization, 2026. URL <https://arxiv.org/abs/2512.16282>.

A. Appendix

A.1. Code

<https://anonymous.4open.science/r/HeRo-Q-3775>

A.2. HeRo-Q Hyperparameters List

To ensure the reproducibility of our experiments, we provide a detailed list of the hyperparameters used in the Smoothing Factor Search and Rotation Optimization phases of HeRo-Q in Table 8. All optimization processes were conducted on an NVIDIA A800 GPU.

For the smoothing factor α , we employ a grid search strategy, scanning the interval $[0, 0.8]$ with a step size of 0.01. For the optimization of the rotation matrix \mathbf{R} , we utilize the Cayley SGD algorithm, performing iterative updates for a fixed number of steps on the calibration data. Unless otherwise specified, the C4 dataset is used for calibration across all experiments.

Category	Hyperparameter	Value / Setting
Smoothing Search	Search Grid \mathcal{A}	$\{0, 0.1, 0.2, \dots, 0.8\}$
	Search Metric	MSE of layer output
Rotation Optimization	Optimizer	Cayley SGD
	Learning Rate (η)	0.01
	Optimization Steps (T_{steps})	200
	Momentum	0.9
	Batch Size	32
Calibration Data	Dataset	C4
	Number of Samples	128
	Sequence Length	2048

Table 8. List of hyperparameters used in HeRo-Q optimization and quantization.

A.3. Theoretical Analysis of Quantization Error Bound

Let $\mathbf{w} \in \mathbb{R}^d$ denote the vectorized parameters of the pre-trained model, and $\hat{\mathbf{w}}$ be the quantized counterpart. We define the quantization perturbation vector as $\boldsymbol{\delta} \triangleq \hat{\mathbf{w}} - \mathbf{w}$.

Given that the pre-trained model has converged to a local minimum, the gradient vanishes ($\nabla \mathcal{L}(\mathbf{w}) \approx \mathbf{0}$). Consequently, the objective degradation $\Delta \mathcal{L}$ is governed by the second-order Taylor expansion:

$$\Delta \mathcal{L} = \mathcal{L}(\mathbf{w} + \boldsymbol{\delta}) - \mathcal{L}(\mathbf{w}) \approx \frac{1}{2} \boldsymbol{\delta}^T \mathbf{H} \boldsymbol{\delta} \quad (6)$$

where $\mathbf{H} \triangleq \nabla^2 \mathcal{L}(\mathbf{w}) \in \mathbb{R}^{d \times d}$ is the Hessian matrix, representing the local curvature of the loss landscape.

A.4. Proof of Theorem 3.1

Let $\mathbf{w} \in \mathbb{R}^d$ denote the vectorized parameters of the pre-trained model, and $\hat{\mathbf{w}}$ be the quantized counterpart. We define the quantization perturbation vector as $\boldsymbol{\delta} \triangleq \hat{\mathbf{w}} - \mathbf{w}$.

Given that the pre-trained model has converged to a local minimum, the gradient vanishes ($\nabla \mathcal{L}(\mathbf{w}) \approx \mathbf{0}$). Consequently, the objective degradation $\Delta \mathcal{L}$ is governed by the second-order Taylor expansion:

$$\Delta \mathcal{L} = \mathcal{L}(\mathbf{w} + \boldsymbol{\delta}) - \mathcal{L}(\mathbf{w}) \approx \frac{1}{2} \boldsymbol{\delta}^T \mathbf{H} \boldsymbol{\delta} \quad (7)$$

where $\mathbf{H} \triangleq \nabla^2 \mathcal{L}(\mathbf{w}) \in \mathbb{R}^{d \times d}$ is the Hessian matrix, representing the local curvature of the loss landscape.

Since the Hessian \mathbf{H} is real and symmetric, the Spectral Theorem guarantees that it admits an eigendecomposition of the form:

$$\mathbf{H} = \mathbf{Q}\Lambda\mathbf{Q}^T \quad (8)$$

where $\mathbf{Q} \in \mathbb{R}^{d \times d}$ is an orthogonal matrix satisfying $\mathbf{Q}^T\mathbf{Q} = \mathbf{I}_d$, and $\Lambda = \text{diag}(\lambda_1, \dots, \lambda_d)$ denotes the diagonal matrix of eigenvalues. Substituting this into Eq. (7) yields:

$$\boldsymbol{\delta}^T \mathbf{H} \boldsymbol{\delta} = \boldsymbol{\delta}^T (\mathbf{Q}\Lambda\mathbf{Q}^T) \boldsymbol{\delta} = (\mathbf{Q}^T \boldsymbol{\delta})^T \Lambda (\mathbf{Q}^T \boldsymbol{\delta}) \quad (9)$$

Let $\mathbf{y} \triangleq \mathbf{Q}^T \boldsymbol{\delta} = [y_1, \dots, y_d]^T$ represent the projection of the noise vector onto the eigenvector basis. The quadratic form can be explicitly expanded via matrix operations:

$$\begin{aligned} \mathbf{y}^T \Lambda \mathbf{y} &= [y_1 \ \dots \ y_d] \begin{bmatrix} \lambda_1 & & 0 \\ & \ddots & \\ 0 & & \lambda_d \end{bmatrix} \begin{bmatrix} y_1 \\ \vdots \\ y_d \end{bmatrix} \\ &= \sum_{k=1}^d \lambda_k y_k^2 \end{aligned} \quad (10)$$

To rigorously derive the worst-case upper bound, we bound the sum by the spectral radius defined as $\lambda_{\max}(\mathbf{H}) \triangleq \max_k |\lambda_k|$. By invoking the property that $\lambda_k \leq \lambda_{\max}(\mathbf{H})$ for all k , and leveraging the unitary invariance of the Euclidean norm under orthogonal transformation ($\|\mathbf{y}\|_2^2 = \|\mathbf{Q}^T \boldsymbol{\delta}\|_2^2 = \|\boldsymbol{\delta}\|_2^2$), we derive the bound as follows:

$$\begin{aligned} \sum_{k=1}^d \lambda_k y_k^2 &\leq \left(\max_j |\lambda_j| \right) \sum_{k=1}^d y_k^2 \\ &= \lambda_{\max}(\mathbf{H}) \|\mathbf{y}\|_2^2 \\ &= \lambda_{\max}(\mathbf{H}) \|\boldsymbol{\delta}\|_2^2 \end{aligned} \quad (11)$$

Consequently, the quantization loss is strictly bounded by the Hessian's spectral radius. This derivation concludes the proof for the following theorem stated in the main text:

Theorem A.1 (Spectral Error Bound). *The worst-case degradation of the objective function is strictly bounded by the product of the Hessian's spectral radius and the squared norm of the quantization perturbation:*

$$\Delta \mathcal{L} \leq \frac{1}{2} \lambda_{\max}(\mathbf{H}) \|\boldsymbol{\delta}\|_2^2 \quad (12)$$

A.5. Proof of Theorem 3.2

In this section, we provide the complete constructive proof of Theorem 3.2. We demonstrate how the HeRo-Q transformation $T \triangleq D_{\alpha}^{-1} R$ achieves a strictly tighter error upper bound by decoupling and synergistically optimizing the ‘Geometric Factor’ and ‘Noise Factor’ within the quantization error bound.

In LLMs, the geometric structure of the loss landscape exhibits extreme anisotropy. Specifically, the spectrum of the Hessian matrix H possesses a tiny number of extremely large eigenvalues, which determine the spectral radius $\lambda_{\max}(H)$ of the matrix. Consequently, the LLM Hessian matrix follows a long-tail distribution. We provide a rigorous mathematical definition as follows:

Definition A.1 (Hessian Diagonal Long-tail) Let H be a $d \times d$ Hessian matrix, with its diagonal elements ordered by magnitude as $|H_{(1)}| \geq |H_{(2)}| \geq \dots \geq |H_{(d)}|$. A significant eigenvalue gap exists, such that a few elements dominate the numerical distribution. Specifically, there exists a non-empty set of outlier indices $\mathcal{S}_{out} = \{k \mid |H_{kk}| \gg 1\}$, such that for

any $k \in \mathcal{S}_{out}$, $|H_{kk}| > 10^3$ or even higher. The maximum value $|H_{(1)}|$ is far greater than the overall level of the spectral distribution, satisfying the following condition:

$$|H_{(1)}| \gg \frac{1}{d} \sum_{i=1}^d |H_{ii}| \quad (13)$$

This long-tail characteristic corresponds geometrically to an extremely elongated "hyper-ellipsoid" loss landscape. The short axes (high-curvature directions) are extremely short and steep, while most directions (low-curvature directions) are very flat.

The core logic of HeRo-Q is to selectively attenuate the curvature of these few long-tail directions through diagonal smoothing D_α , thereby fundamentally reducing the model's sensitivity to quantization noise.

A.5.1. GENERALIZED ERROR BOUND IN TRANSFORMED SPACE

To address the norm scaling issues inherent in non-unitary transformations, we first reconstruct the second-order loss approximation within the transformed coordinate system.

Let \mathbf{w} denote the original weights and $\tilde{\mathbf{w}} = T^{-1}\mathbf{w}$ be the transformed weights. The quantization operation $Q(\cdot)$ is executed in this transformed space, resulting in the quantization noise vector $\tilde{\boldsymbol{\delta}} \triangleq Q(\tilde{\mathbf{w}}) - \tilde{\mathbf{w}}$.

According to the Taylor expansion, the loss degradation $\Delta\mathcal{L}$ recovered in the original space is governed by:

$$\Delta\mathcal{L} \approx \frac{1}{2}(T\tilde{\boldsymbol{\delta}})^T \mathbf{H}(T\tilde{\boldsymbol{\delta}}) = \frac{1}{2}\tilde{\boldsymbol{\delta}}^T (T^T \mathbf{H} T)\tilde{\boldsymbol{\delta}} = \frac{1}{2}\tilde{\boldsymbol{\delta}}^T \tilde{\mathbf{H}}\tilde{\boldsymbol{\delta}} \quad (14)$$

where $\tilde{\mathbf{H}} \triangleq T^T \mathbf{H} T$ is defined as the *equivalent Hessian matrix*.

Utilizing the spectral norm property $(\mathbf{x}^T \mathbf{A} \mathbf{x} \leq \lambda_{\max}(\mathbf{A}) \|\mathbf{x}\|_2^2)$, we derive the total error upper bound:

$$\Delta\mathcal{L} \leq \frac{1}{2} \underbrace{\lambda_{\max}(\tilde{\mathbf{H}})}_{\text{Geometric Factor}} \cdot \underbrace{\|\tilde{\boldsymbol{\delta}}\|_2^2}_{\text{Noise Factor}} \quad (15)$$

The core of the proof lies in demonstrating that HeRo-Q can jointly minimize the product of these two factors. Expanding the definition of the equivalent Hessian $\tilde{\mathbf{H}}$ using $T = D_\alpha^{-1}R$ yields:

$$\tilde{\mathbf{H}} = (D_\alpha^{-1}R)^T \mathbf{H} (D_\alpha^{-1}R) = R^T (D_\alpha^{-1} \mathbf{H} D_\alpha^{-1}) R = R^T \hat{\mathbf{H}} R \quad (16)$$

Since R is an orthogonal matrix ($R^T = R^{-1}$), the relation $\tilde{\mathbf{H}} = R^{-1} \hat{\mathbf{H}} R$ constitutes a *similarity transformation*. Fundamental linear algebra dictates that similarity transformations preserve the eigenvalues of a matrix. Consequently, the spectral properties of $\tilde{\mathbf{H}}$ remain identical to those of the diagonally scaled matrix $\hat{\mathbf{H}}$, regardless of the rotation R .

Thus, the equivalent Hessian $\tilde{\mathbf{H}}$ and the preconditioned Hessian $\hat{\mathbf{H}}$ share the same spectral radius:

$$\lambda_{\max}(\tilde{\mathbf{H}}) = \lambda_{\max}(\hat{\mathbf{H}}) \quad (17)$$

This establishes that the optimization of the Geometric Factor can be simplified to the analysis of $\hat{\mathbf{H}}$, independent of the rotation matrix R .

Considering the element at the k -th row and j -th column, denoted as \hat{H}_{kj} , we perform the matrix multiplication $\hat{\mathbf{H}} = \mathbf{D}_\alpha^{-1} \mathbf{H} \mathbf{D}_\alpha^{-1}$:

$$\hat{H}_{kj} = \sum_m \sum_n (D_\alpha^{-1})_{km} H_{mn} (D_\alpha^{-1})_{nj} \quad (18)$$

Given that D_α^{-1} is diagonal, the sums collapse to single non-zero terms where $m = k$ and $n = j$:

$$\hat{H}_{kj} = (D_\alpha^{-1})_{kk} H_{kj} (D_\alpha^{-1})_{jj} \quad (19)$$

Substituting the scaling factor $(D_\alpha^{-1})_{ii} = 1/|H_{ii}|^{\alpha/2}$:

$$\hat{H}_{kj} = \frac{1}{|H_{kk}|^{\alpha/2}} \cdot H_{kj} \cdot \frac{1}{|H_{jj}|^{\alpha/2}} = \frac{H_{kj}}{|H_{kk}|^{\alpha/2} |H_{jj}|^{\alpha/2}} \quad (20)$$

This explicit form serves as the basis for the subsequent bound derivation. By analyzing the absolute row sums of the equivalent matrix, a strict upper bound for the spectral radius $\lambda_{\max}(\hat{\mathbf{H}})$ can be derived:

Theorem A.2 (Spectral Radius Upper Bound). *The spectral radius $\lambda_{\max}(\hat{\mathbf{H}})$ is strictly bounded by the maximum absolute row sum:*

$$\lambda_{\max}(\hat{\mathbf{H}}) \leq \max_k \left(|\hat{H}_{kk}| + \sum_{j \neq k} |\hat{H}_{kj}| \right) \quad (21)$$

Proof. Let (λ, \mathbf{x}) be an eigenpair of $\hat{\mathbf{H}}$, normalized such that the magnitude of the maximum component is 1 (i.e., $|x_k| = 1$, implying $|x_j| \leq 1$ for all j).

Starting from the k -th row of the eigenvalue equation $\sum_j \hat{H}_{kj} x_j = \lambda x_k$, we isolate the term involving λ :

$$(\lambda - \hat{H}_{kk}) x_k = \sum_{j \neq k} \hat{H}_{kj} x_j \quad (22)$$

Taking the absolute value on both sides and applying the Triangle Inequality:

$$|\lambda - \hat{H}_{kk}| \cdot 1 = \left| \sum_{j \neq k} \hat{H}_{kj} x_j \right| \leq \sum_{j \neq k} |\hat{H}_{kj}| \cdot |x_j| \leq \sum_{j \neq k} |\hat{H}_{kj}| \quad (23)$$

Applying the Reverse Triangle Inequality ($|\lambda| - |\hat{H}_{kk}| \leq |\lambda - \hat{H}_{kk}|$) yields:

$$|\lambda| \leq |\hat{H}_{kk}| + \sum_{j \neq k} |\hat{H}_{kj}| \quad (24)$$

Since this inequality holds for any eigenvalue, it must hold for the spectral radius. \square

Substituting $|\hat{H}_{kk}| = |H_{kk}|^{1-\alpha}$ and the off-diagonal forms into the above results in the final theorem:

Theorem A.3 (Spectral Radius Compression Theorem). *The spectral radius of the Hessian after HeRo-Q transformation is strictly bounded by the following surrogate objective function $\mathcal{B}(\alpha)$:*

$$\lambda_{\max}(\tilde{\mathbf{H}}) \leq \max_k \left(|H_{kk}|^{1-\alpha} + \sum_{j \neq k} \frac{|H_{kj}|}{|H_{kk}|^{\alpha/2} |H_{jj}|^{\alpha/2}} \right) \triangleq \mathcal{B}(\alpha) \quad (25)$$

Based on **Definition A.1**, the spectral radius is determined by a small number of outlier indices $k \in \mathcal{S}_{out}$, whose core characteristic is that their diagonal magnitudes are significantly greater than unity ($|H_{kk}| \gg 1$). For the rows $k \in \mathcal{S}_{out}$ that dominate the spectral radius, we observe the variation of the two components as α increases:

Exponential Reduction of the Diagonal Term: Given the base $|H_{kk}| \gg 1$, the function $g(\alpha) = |H_{kk}|^{1-\alpha}$ is an exponentially decaying function with respect to the base $|H_{kk}|$. As α increases from 0, this term decreases at an extremely rapid rate.

Smoothing Suppression of Off-diagonal Terms: For the off-diagonal sum $\sum_{j \neq k} \frac{|H_{kj}|}{(|H_{kk}| |H_{jj}|)^{\alpha/2}}$, since the product $|H_{kk}| |H_{jj}|$ is also significantly greater than 1 (guaranteed by the long-tail assumption), the denominator grows exponentially as α increases. Consequently, the sum of the entire off-diagonal components strictly decreases.

Since every component of the surrogate function $\mathcal{B}(\alpha)$ behaves as a strictly decreasing function of α under the condition $|H_{kk}| \gg 1$, it follows that $\mathcal{B}(\alpha)$ must be monotonically decreasing within the initial interval $\alpha \in (0, \alpha^*]$.

Through the analysis above, we have formally proven Theorem 3.2 (Spectral Compression Guarantee) in the main text: under the assumption that the LLM Hessian satisfies the diagonal long-tail distribution, there exists an interval where the loss upper bound after the HeRo-Q transformation is strictly lower than the untreated baseline.

$$\exists \alpha^* > 0 \text{ s.t. } \mathcal{B}(\alpha^*) < \mathcal{B}(0). \quad (26)$$

This theoretical result perfectly supports the first half of the U-shaped curve observed in experiments, demonstrating the decisive role of the smoothing mechanism in suppressing pathological curvature.

A.6. Formal Analysis of Noise Factor: Outlier Amplification and Suppression

While the smoothing parameter α successfully compresses the Geometric Factor $\mathcal{B}(\alpha)$ by reducing the Hessian's spectral radius, the quantization noise norm $\|\tilde{\delta}\|_2^2$ in the transformed space is not invariant. We analyze this phenomenon through the lens of *inference equivalence*.

To maintain the output of the linear layer $\mathbf{Y} = \mathbf{X}\mathbf{W}$ after introducing the transformation \mathbf{T} , the following identity must hold:

$$\mathbf{Y} = \mathbf{X}\mathbf{I}\mathbf{W} = (\mathbf{X}\mathbf{T})(\mathbf{T}^{-1}\mathbf{W}) = \tilde{\mathbf{X}}\tilde{\mathbf{W}} \quad (27)$$

Consequently, the transformed weights to be quantized are defined as $\tilde{\mathbf{W}} = \mathbf{T}^{-1}\mathbf{W}$. Substituting the definition $\mathbf{T} = \mathbf{D}_\alpha^{-1}\mathbf{R}$ and applying the matrix inversion rule $(\mathbf{AB})^{-1} = \mathbf{B}^{-1}\mathbf{A}^{-1}$ along with the orthogonality of the rotation matrix ($\mathbf{R}^{-1} = \mathbf{R}^\top$), we derive the transformed weights as:

$$\tilde{\mathbf{W}} = (\mathbf{D}_\alpha^{-1}\mathbf{R})^{-1}\mathbf{W} = \mathbf{R}^\top \mathbf{D}_\alpha \mathbf{W} \quad (28)$$

Given the diagonal smoothing matrix $\mathbf{D}_\alpha = \text{diag}(|H_{ii}|^{\alpha/2})$, increasing α effectively attenuates the Hessian eigenvalues in the curvature space. However, due to the inverse relationship, it acts as a direct scaling amplifier in the weight space. This non-uniform scaling leads to a significant expansion of the L_∞ norm of the weight vector:

$$\|\tilde{\mathbf{W}}\|_\infty \propto \max_k \left(|H_{kk}|^{\alpha/2} |W_k| \right) \quad (29)$$

Since Large Language Models (LLMs) exhibit extreme outliers ($|H_{kk}| \gg 1$), even a marginal increase in α forces the quantizer to adopt a larger step size Δ to cover the drastically expanded dynamic range. This results in a quadratic growth of the expected quantization noise variance:

$$\mathbb{E}[\|\tilde{\delta}\|_2^2] \propto \Delta^2 \propto \|\tilde{\mathbf{W}}\|_\infty^2 \quad (30)$$

Thus, Theorem 3.2 formalizes a fundamental optimization problem: finding the optimal α^* to balance the gain from ‘spectral radius compression’ against the cost of ‘dynamic range expansion.’ This explains the U-shaped performance curve observed in experiments:

Insufficient compression of the Hessian spectral radius $\lambda_{\max}(\tilde{\mathbf{H}})$ makes the model highly sensitive to even minor quantization noise. Excessive expansion of the weight dynamic range causes the *Noise Factor* to dominate, degrading performance through increased clipping and rounding errors.

As the Geometric Factor $\mathcal{B}(\alpha)$ is invariant to the rotation \mathbf{R} , the role of \mathbf{R} is strictly decoupled to minimize the Noise Factor by redistributing weight energy more uniformly across channels:

$$\mathbf{R}^* = \arg \min_{\mathbf{R} \in SO(d)} \|\text{Quantize}(\mathbf{R}^\top \mathbf{D}_\alpha \mathbf{W}) - \mathbf{R}^\top \mathbf{D}_\alpha \mathbf{W}\|_2^2 \quad (31)$$

A.7. Inference overhead

As illustrated in Figure 6, HeRo-Q adopts a hybrid inference strategy that strictly distinguishes between mergeable transformations (offline fusion) and online transformations to minimize runtime latency.

For the vast majority of linear layers (e.g., the Query/Key/Value projections in Attention blocks and the Up/Gate/Down projections in MLP blocks), the transformation matrix $\mathbf{T} \triangleq \mathbf{D}_\alpha^{-1}\mathbf{R}$ can be mathematically fused into the adjacent weight

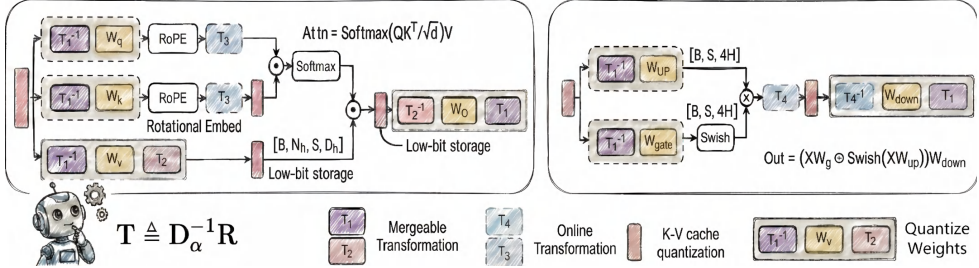


Figure 6. Overview of the HeRo-Q Inference Pipeline. We adopt a hybrid deployment strategy for the transformation $\mathbf{T} \triangleq \mathbf{D}_\alpha^{-1} \mathbf{R}$. Purple blocks denote mergeable transformations, where \mathbf{T} or \mathbf{T}^{-1} is fused offline into the adjacent weights ($\mathbf{W}_{q,k,v,o}$ and MLP weights), incurring zero runtime overhead. Grey blocks indicate *online transformations* required where structural fusion is blocked (before RoPE or for KV-cache quantization), which are executed efficiently using optimized kernels.

matrices before inference. As shown in the purple blocks in Figure 6, we apply the following equivalent structural re-parameterization:

The inverse smoothing diagonal \mathbf{D}_α^{-1} is absorbed into the preceding normalization layers (LayerNorm). This is a standard element-wise rescaling that incurs no additional operators.

The dense rotation matrix \mathbf{R} is fused into the weight matrices. For a linear layer $\mathbf{Y} = \mathbf{XW}$, the operation becomes $\mathbf{Y} = (\mathbf{XR})(\mathbf{R}^\top \mathbf{W})$. We pre-compute $\mathbf{W}' = \mathbf{R}^\top \mathbf{W}$ offline. Similarly, the preceding layer’s output weights are updated to $\mathbf{W}'_{prev} = \mathbf{W}_{prev} \mathbf{R}$ to produce the rotated activation \mathbf{XR} .

Since these operations are completed during the model saving phase, the inference-time computational complexity for these layers remains strictly unchanged at $\mathcal{O}(0)$ additional cost.

In specific scenarios where weight fusion is structurally blocked—such as the Key-Value (KV) Cache quantization or activations preceding Rotary Positional Embeddings (RoPE)—we employ online transformations (depicted as grey blocks in Figure 6). To prevent the $\mathcal{O}(d^2)$ complexity of standard matrix multiplication from becoming a bottleneck, we follow the approach of SpinQuant by adopting *Hadamard Rotation*. By utilizing the Fast Walsh-Hadamard Transform (FWHT) kernel, the time complexity of the online rotation is reduced from quadratic to log-linear:

$$\text{Complexity: } \mathcal{O}(d^2) \rightarrow \mathcal{O}(d \log d) \quad (32)$$

where d is the hidden dimension. Given that $d \log d \ll d^2$ for large language models, this overhead is negligible compared to the heavy GEMM (General Matrix Multiply) operations in linear layers. Consequently, HeRo-Q achieves inference throughput comparable to standard FP16 and GPTQ baselines, as empirically verified in Table 5.

A.8. Calibration Cost Analysis

While HeRo-Q introduces an iterative optimization phase to learn the rotation matrix R , we demonstrate that its calibration overhead remains within a highly practical range for industrial deployment. We evaluated the wall-clock time and peak GPU memory usage during the quantization calibration phase on a single NVIDIA A800 (80GB) GPU. The results, compared with standard baselines, are summarized in Table 9.

Category	Method	Time	Peak VRAM
Baselines	GPTQ	~25 mins	~16 GB
	OmniQuant	~74 mins	~30 GB
Ours	HeRo-Q	~38 mins	~24 GB

Table 9. Comparison of quantization time and memory cost on Llama-3-8B (NVIDIA A800).

In terms of computational efficiency, the total time cost to calibrate the Llama-3-8B model using HeRo-Q is approximately 38 minutes. Although compared to the gradient-free baseline method GPTQ (25 minutes), which relies solely on closed-form Hessian inversion, HeRo-Q indeed brings a moderate increase in latency, this additional cost is fully justified. This is because

we obtained critical performance gains in the ultra-low-bit regime, such as effectively preventing model collapse under W3A16 settings. Furthermore, when compared with other optimization-based quantization frameworks like OmniQuant—the latter requiring extensive gradient updates for learnable clipping and weights (74 minutes)—HeRo-Q achieved a significant 1.9x speedup. This high efficiency stems from our streamlined optimization objective: we exclusively optimize the orthogonal rotation matrix R for a limited budget of 200 steps per layer, thereby avoiding the heavy computational burden brought by full-parameter fine-tuning while ensuring fast convergence.

In terms of memory footprint, HeRo-Q exhibits remarkable resource efficiency, requiring only approximately 24 GB of peak VRAM during the calibration phase. This figure is significantly lower than the memory demand of OmniQuant (30 GB), and crucially, it falls completely within the memory capacity range of high-end consumer-grade GPUs such as the NVIDIA RTX 3090 or 4090. This characteristic significantly democratizes access to high-performance quantization, enabling the algorithm to be deployed on accessible hardware without strict reliance on data center-grade infrastructure.